WS$_2$ quantum dots/MoS$_2$@WO$_{3-x}$ core-shell hierarchical dual Z-scheme tandem heterojunctions with wide-spectrum response and enhanced photocatalytic performance

Meijun Guo[a], Zipeng Xing[a,*], Tianyu Zhao[a], Zhenzi Li[b,*], Shilin Yang[a], Wei Zhou[a,*]

[a] Department of Environmental Science, School of Chemistry and Materials Science, Key Laboratory of Functional Inorganic Material Chemistry, Ministry of Education of the People's Republic of China, Heilongjiang University, Harbin 150080, PR China
[b] Department of Epidemiology and Biostatistics, Harbin Medical University, Harbin 150086, PR China

ABSTRACT

A novel WS$_2$/MoS$_2$@WO$_{3-x}$ core-shell hierarchical dual Z-scheme tandem heterojunction photocatalyst is fabricated through two-step hydrothermal and heat-treatment strategy. The unique dual Z-scheme tandem heterojunction core-shell structure favors the transfer and spatial separation of photogenerated electron-hole pairs greatly, in which WO$_{3-x}$ serves as a bridge to connect two semiconductors and extends the photoresponse to visible light and NIR regions. The obtained core-shell structure tandem heterojunction exhibits excellent photothermal and photocatalytic performance, which is much better than that of any pristine ones. The excellent activity can be ascribed to the dual Z-scheme tandem heterojunction favoring transfer and spatial separation of photogenerated charge carriers, surface defect engineering (oxygen doping) extending photoresponse to long wavelength region and prolonging the lifetime of carriers, and the hierarchical structure offering massive surface active sites. In addition, the photothermal effect for the tandem heterojunction promotes the photocatalytic performance obviously.

1. Introduction

In recent decades, the inadequacy of freshwater resources has become more and more serious on account of the increasing environmental pollution [1–3]. As an advanced technology, photocatalytic technology becomes a promising and economical method to solve this issue because the solar energy is the most abundant resource in the earth [4–7]. Solar to thermal conversion has recently attracted lots of interests. Recently, photothermal materials are rapidly becoming a growing area of photothermal water vaporization for clean water [8–10]. Qiao et al. prepared a floating Ag nanoparticle/carbon cloth with solar to thermal conversion, which could effectively evaporate seawater and treat sewage [11]. Gan et al. prepared a photocatalyst with photothermal effect, which proved that photothermal effect could effectively improve the photocatalytic performance [12]. Therefore, the combined use of photothermal conversion and photocatalysis to treat sewage is a novel direction of great research value.

Among recently reported photocatalytic materials, noble-metal-free MoS$_2$ based photocatalysts have received lots of attention due to the unique chemical and physical properties [13–15]. In addition, MoS$_2$

materials have excellent optical absorption and photothermal property [16,17]. Therefore, MoS$_2$ is often combined with other photocatalysts to prepare high performance photocatalysts. Recently, Hu et al. prepared a composite photocatalyst by selectively depositing MoS$_2$ nanosheets onto exposed high-active facets of TiO$_2$, which has excellent photocatalytic hydrogen production performance [14]. Typically, MoS$_2$ is a layered structure (S-Mo-S) stacked by weak van der Waals forces and the crystal structures of MoS$_2$ are defined into four types: 1 T, 1H, 2H, and 3R [18–20]. The unsaturated S atoms at the edges of MoS$_2$ nanosheets are the key to photocatalytic activity, while the S atoms in the bulk of MoS$_2$ have no activity [21–23]. Herein, the synthesis of MoS$_2$ with a large number of edges and active S atoms is an effective method to improve the photocatalytic performance [24]. Moreover, the incorporated O atoms in MoS$_2$ nanosheets that simply derived from the inert Mo-O bonding of the precursor could well enhance the conductivity of the MoS$_2$ sheets [25,26].

Recently, WO$_3$ is often used for water oxidation, photocatalytic degradation, and photocatalytic H$_2$ evolution [27,28]. WO$_3$ with a broad range of band-gap values (2.4–2.8 eV) is non-toxic, economical and photo-corrosion resistant. Furthermore, the stability of WO$_3$ under

* Corresponding authors.
  E-mail addresses: xingzipeng@hlju.edu.cn (Z. Xing), zhenzhenlee2014@163.com (Z. Li), zwchem@hotmail.com (W. Zhou).

acidic and oxidation conditions is impressive [29]. WO_3 can be easily synthesized into two-dimensional structures, which expose the high-energy facets [30]. However, the photocatalytic activity of WO_3 is still unsatisfactory due to narrowed light absorption range and the rapid recombination of photogenerated electron-hole pairs [31]. Herein, compounding WO_3 with other semiconductor materials is an effective way to improve photocatalytic performance [31,32]. Shi et al. reported that Cu_2O decorated WO_3 nanosheets with dominant (001) facets could effectively enhance photocatalytic CO_2 reduction under visible light irradiation [29]. Wang et al. prepared two-dimensional heterostructures of WO_3 and WC to effectively photodegrade organic pollutants under vis-NIR irradiation [33]. Moreover, oxygen vacancies in WO_{3-x} serve as shallow donors to improve the electrical conductivity and donor density, and enhance the adsorption of surface species, making WO_x family promising as photocatalysts and electrode materials [34]. Furthermore, WS_2 has recently been used as a photocatalyst [35]. WS_2 is a non-noble metal semiconductor material with wide spectral response. Furthermore, the structure of WS_2 is similar to that of MoS_2 [24,36]. It is often used as a co-catalyst in combination with another semiconductor photocatalysts [37]. Gopannagari et al. reported the composite of few-layered WS_2 nanosheets and CdS nanorods can effectively prolong the lifetime of photogenerated carriers and enhance the surface shuttling properties via active edge sites and superior intrinsic electrical conductivity [38]. Therefore, the formation of heterojunction is an effective way to improve the photocatalytic performance.

In this work, we prepare WS_2 quantum dots/MoS_2@WO_{3-x} nanospheres with broad solar absorption, using two-step hydrothermal and calcination method. WS_2/MoS_2@WO_{3-x} shows unique core-shell structure of hierarchical nanospheres with dual Z-scheme through reasonable design of morphological structure and band structure. WS_2/MoS_2@WO_{3-x} core-shell tandem heterojunctions exhibit efficient solar light harvesting and photothermal effect. In addition, the as-prepared photocatalysts are characterized in detail and the possible photocatalytic mechanism is also proposed. The separation and transfer efficiency of photoinduced carriers can be improved by reasonable structure design, suitable energy band location and surface defect engineering, which opens up a simple and effective strategy for the design and practical application of highly active visible light photocatalysts.

2. Experimental section

Detailed experiments are included in the Supplementary Material. The synthesis process of WS_2 Quantum Dots/MoS_2@WO_{3-x} core-shell heterojunctions is shown in Scheme 1. First, MoS_2 nanospheres were prepared. Then, MoS_2 nanospheres were added to the solution containing the precursor of WO_{3-x} to obtain MoS_2@WO_{3-x} core-shell nanospheres. Subsequently, the MoS_2@WO_{3-x} nanospheres were added into the suspension containing WS_2 quantum dots. Ultimately, the soaked products were calcined to obtain the final WS_2/MoS_2@WO_{3-x} products.

3. Results and discussion

As shown in Fig. 1a, for the MoS_2 nanospheres, there are three characteristic XRD diffraction peaks at 12.2, 33.1, and 58.9° respectively, which can be assigned to (002), (100), and (110) planes [24,39]. It is noteworthy that the characteristic peak at 12.2° of MoS_2 nanospheres has a blue shift compared with pristine MoS_2 phase (JCPDS No. 75-1539), which indicates that a lamellar structure with larger lattice spacing is formed [18]. Fig. 1b shows the increase of the lattice spacing in the atomic schematic diagram. The lattice fringe spacing of (002) planes of MoS_2 prepared by conventional method is 0.62 nm [13,40], however, the lattice fringes of (002) planes become larger when the defects are formed in MoS_2. This is due to the low reaction temperature of the synthesis process of MoS_2 nanospheres, resulting in O doping into

the lattice [40]. Furthermore, the characteristic peaks of MoS_2@WO_{3-x} include the characteristic peaks of MoS_2 and WO_3 [31]. This result shows that WO_{3-x} is successfully loaded on the surface of MoS_2 nanospheres. After loading WS_2 QDs, no characteristic peaks of photocatalyst is changed significantly, which may be due to the small particle size and low content of WS_2 QDs. Therefore, the XRD diffraction peaks of WS_2 QDs cannot be observed obviously for WS_2/MoS_2@WO_{3-x}. Furthermore, to further verify the composition, Raman measurements are carried out. As shown in Figure S1, WS_2/MoS_2@WO_{3-x} shows the characteristic peaks of WS_2, MoS_2, and WO_{3-x}, which identified the successful combination of WS_2/MoS_2@WO_{3-x}.

As shown in Fig. 2a, it can be seen that the MoS_2 nanospheres are composed of layered MoS_2. Furthermore, the MoS_2 nanospheres are uniform in size, with a main diameter of about 400 nm. Figs. 2b and 2c show the TEM images of MoS_2 nanospheres, which also confirm the layered structure of nanospheres. Fig. 2c shows the (002) interplanar spacing of the MoS_2 nanospheres with a spacing of 0.67 nm, which is larger than the lattice fringes of non-defect MoS_2. According to previous reports, this may be due to the substitution of S by O doping [24]. SEM image of WO_{3-x} is shown in Figure S2, we can observe that pristine WO_{3-x} has a rod-like structure, which is similar to the surface of WS_2/MoS_2@WO_{3-x}. As shown in Fig. 2d, it can be clearly seen that the surface of the nanosphere after loading becomes much rougher and more wrinkled, which indicates that WO_{3-x} is successfully coated on the surface of MoS_2 nanospheres. However, no obvious WS_2 QDs are found, which is due to the small size of WS_2 QDs. In addition, as shown in Figure S3, it can be clearly observed that WO_{3-x} are loaded on the surface of MoS_2 nanospheres to form a core-shell structure and WS_2 QDs are dispersed on the surface of core-shell nanospheres. Fig. 2e further demonstrates the formation of the core-shell MoS_2@WO_{3-x} structure and the distribution of WS_2 QDs on the surface of the core-shell structure. As shown in Fig. 2f, the lattice fringes with a spacing of about 0.38 and 0.67 nm can be assigned to (110) crystal plane of WO_3 and (002) crystal plane of the MoS_2. Furthermore, tiny WS_2 QDs are homogeneously dispersed on the MoS_2@WO_{3-x} as the result of the deposition process and the lattice fringes with a spacing of 0.17 nm can be assigned to the (106) crystal plane of the WS_2. The core-shell WS_2/MoS_2@WO_{3-x} is also analyzed using SEM coupled with energy dispersive X-ray spectroscopy (EDX) to confirm the composition. SEM image of WS_2/MoS_2@WO_{3-x} and EDX maps are shown in Fig. 2g, indicating the composition of photocatalyst with four elements and confirming the core-shell structure. Besides, EDX elemental spectrum of WS_2/MoS_2@WO_{3-x} is shown in Figure S4. It is clearly shown that the WS_2/MoS_2@WO_{3-x} contains W, Mo, O and S, which directly proves the formation of the composites.

The surface chemistry and chemical composition of the composites are analyzed by XPS. In Figure S5, the full XPS spectrum shows that W, O, S, and Mo elements can be clearly observed, which could indicate the co-existence of MoS_2, WO_{3-x}, and WS_2. As shown in Fig. 3a, it can be observed that Mo^{6+} and Mo^{5+} exist in XPS spectra of WS_2/MoS_2@WO_{3-x}, which is consistent with the XRD analysis and further proves the doping of oxygen [25,40]. Furthermore, the high resolution Mo 3d spectra of WS_2/MoS_2@WO_{3-x} displays two peaks at 231.7 and 228.8 eV assigning to Mo^{4+} $3d_{3/2}$ and Mo^{4+} $3d_{5/2}$ [26]. Moreover, the peak centered at 226.3 eV ascribed to S 2s is also observed in Fig. 3a [40]. As shown in Fig. 3b, the W^{6+} $4f_{5/2}$, W^{6+} $4f_{7/2}$, W^{5+} $4f_{5/2}$ and W^{5+} $4f_{7/2}$ at 38.4, 36.3, 37.9 and 35.8 eV, which indicates that WO_{3-x} has been formed [41]. There are two peaks at 34.9 and 32.6 eV, assigning to W^{4+} $4f_{5/2}$ and W^{4+} $4f_{7/2}$ in WS_2 [42]. Furthermore, in Fig. 3c, three characteristic peaks are located at 529.9, 531.4, and 532.1 eV, corresponding to lattice oxygen bound of W-O/Mo-O, −OH, and absorbed H_2O respectively [43]. As shown in Fig. 3d, the S 2p spectrum shows that two characteristic peaks are located at 163.4 and 161.9 eV, corresponding to S^{2-} $2p_{1/2}$ and S^{2-} $2p_{3/2}$ respectively [44].

The photoresponse range of photocatalyst is one of the important factors affecting the performance of photocatalysts. As shown in Fig. 4a,
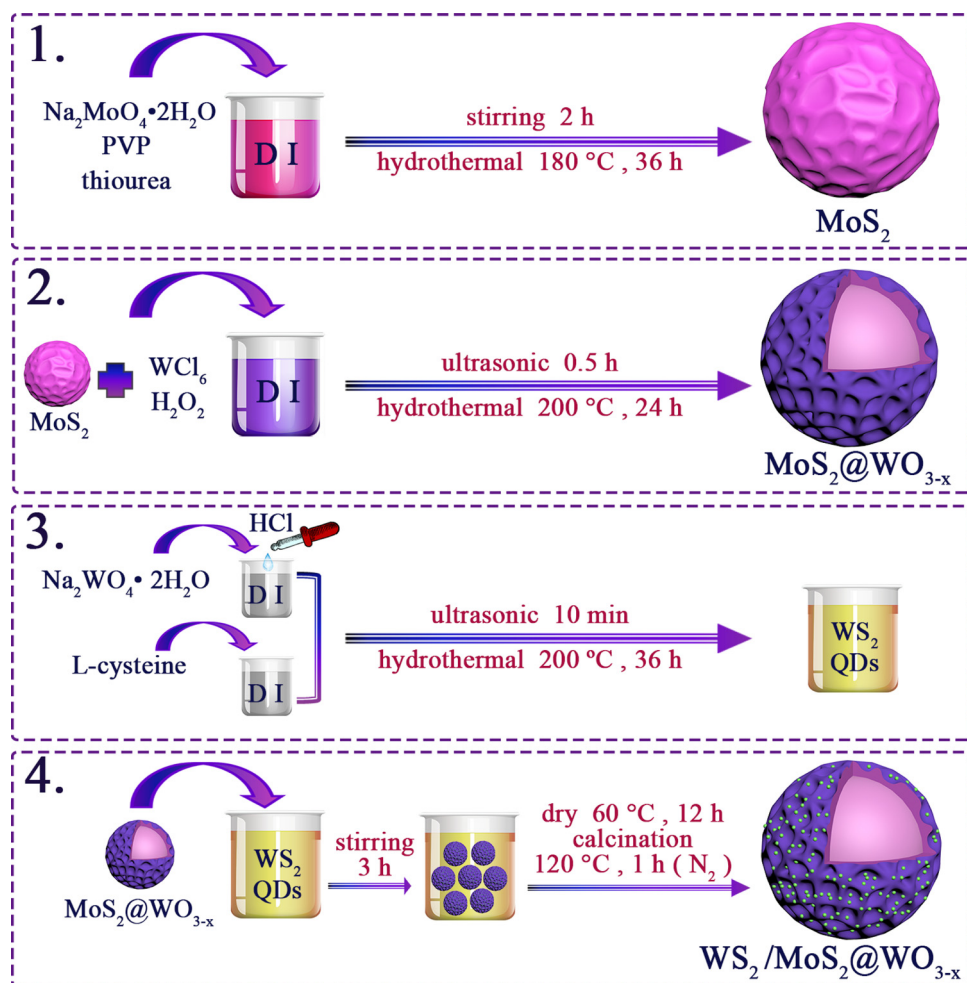
Scheme 1. Schematic diagram for the formation of $WS_2/MoS_2@WO_{3-x}$ heterostructures.

the photoresponse range of MoS_2 nanospheres is from ultraviolet region to infrared region. Furthermore, composite samples ($MoS_2@WO_{3-x}$, WS_2/MoS_2 and $WS_2/MoS_2@WO_{3-x}$) also have strong light absorption in the infrared region, which indicates that they may have photothermal effect. Compared with WO_{3-x}, the photoresponse range of $MoS_2@WO_{3-x}$ is obviously broadened, which is from visible light to infrared region. Moreover, when WS_2 is loaded on the surface of $MoS_2@WO_{3-x}$, the absorption intensity of $WS_2/MoS_2@WO_{3-x}$ in the infrared region is obviously increased. Figure S6 shows the band gap of different photocatalyst, which is calculated by the Kubelka-Munk plots. It is obvious that all the band gaps of semiconductors are narrower than 3 eV, which meet the primary requirement for the construction of a Z-scheme system. As shown in Figure S7, the color of MoS_2, WS_2, $MoS_2@WO_{3-x}$,

WS_2/MoS_2, and $WS_2/MoS_2@WO_{3-x}$ are black, which corresponds to the photoresponse range. Because black materials often have photothermal effect, they have potential application value in photothermal conversion for solar water evaporation. As active species, ·OH participates in photocatalytic degradation. Coumarin can react with ·OH to form 7-hydroxycoumarin with fluorescence property, so the concentration of ·OH can be measured by fluorescence intensity. As shown in Fig. 4b, the ·OH content of $WS_2/MoS_2@WO_{3-x}$ photocatalyst is the highest, which corresponds to the results of photocatalytic degradation. The photocatalytic degradation performance is tested by photodegrade organic pollutant. Fig. 4c shows the experimental results of photocatalytic degradation for 2,4-DCP. In dark reaction experiment, the maximum dark adsorption capacity of MoS_2, $MoS_2@WO_{3-x}$, WS_2/MoS_2, and $WS_2/$

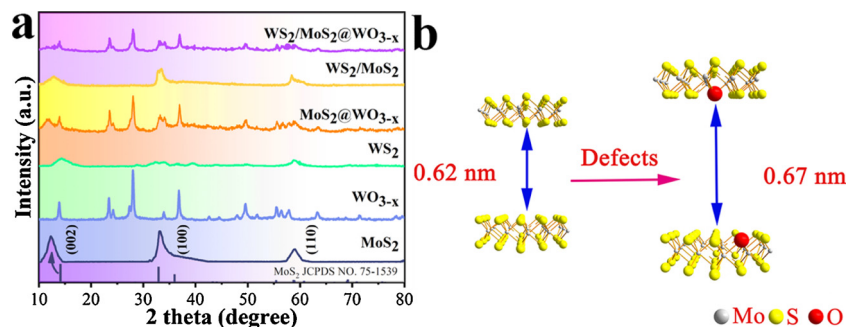**Fig. 1.** Typical XRD patterns (a) of MoS_2, WO_{3-x}, WS_2, $MoS_2@WO_{3-x}$, WS_2/MoS_2, and $WS_2/MoS_2@WO_{3-x}$, respectively. Atomic schematic of the interlayer spacing for defected MoS_2 (b).

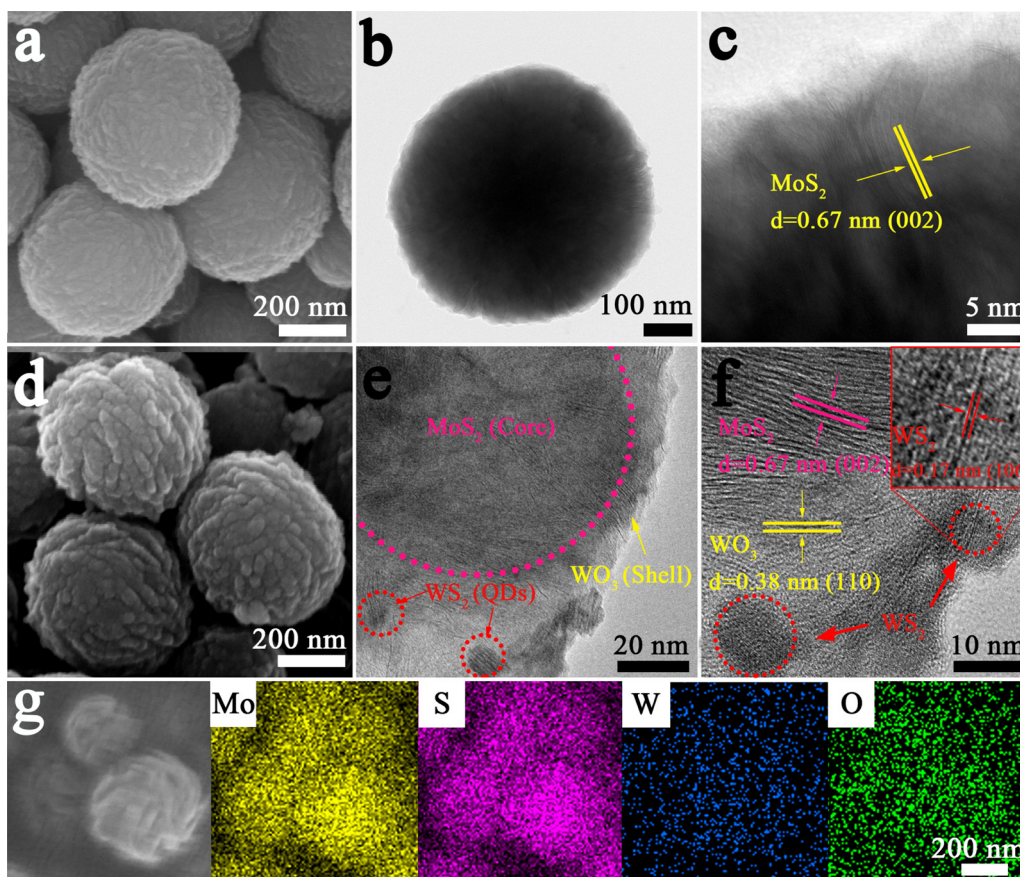**Fig. 2.** SEM images of MoS$_2$ nanospheres (a) and WS$_2$/MoS$_2$@WO$_{3-x}$ (d), TEM images of MoS$_2$ nanospheres (b, c) and WS$_2$/MoS$_2$@WO$_{3-x}$ (e, f), SEM and corresponding EDX maps of Mo, S, W and O elements.
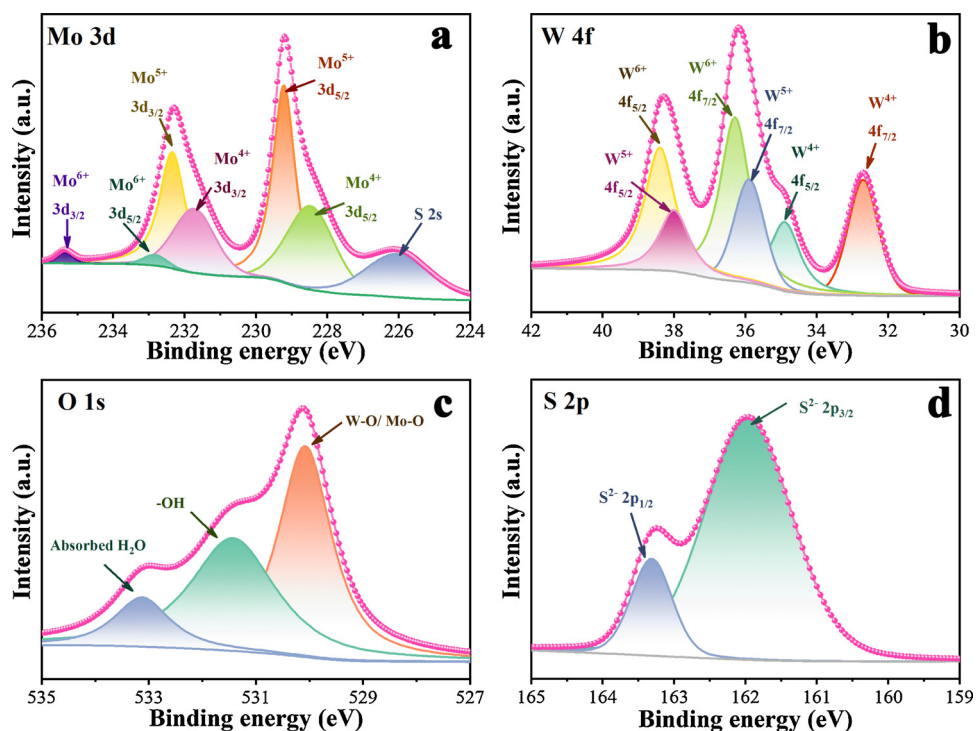

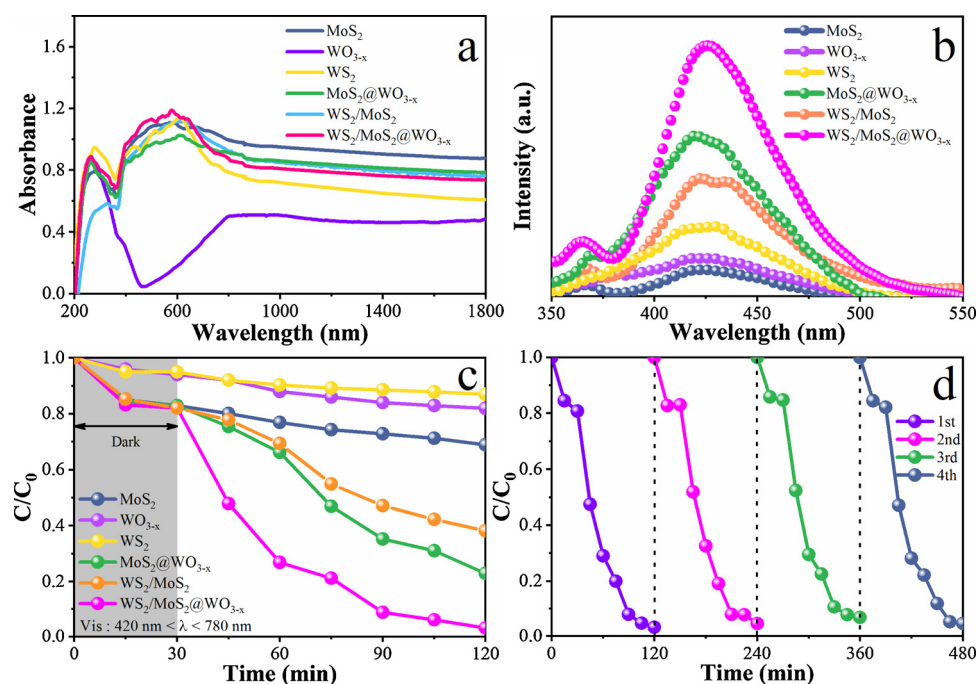**Fig. 3.** High-resolution XPS spectra of Mo 3d (a), W 4f (b), O 1s (c) and S 2p (d) for WS$_2$/MoS$_2$@WO$_{3-x}$, respectively.

Fig. 4. UV–vis DRS spectra (a), fluorescence spectra related to the amount of produced ˙OH (b), photocatalytic degradation of 2,4-DCP of MoS_2, WO_{3-x}, WS_2, $MoS_2@WO_{3-x}$, WS_2/MoS_2 and $WS_2/MoS_2@WO_{3-x}$ (c), and the recycling runs of $WS_2/MoS_2@WO_{3-x}$ for degrading 2,4-DCP (d).

$MoS_2@WO_{3-x}$ is about 20%, and the poor adsorption capacity of WO_{3-x} and WS_2 is 5 and 6%, respectively. The results of dark reaction experiment for 30 min show that the specific surface area of MoS_2, $MoS_2@WO_{3-x}$, WS_2/MoS_2, and $WS_2/MoS_2@WO_{3-x}$ is larger than that of WO_{3-x} and WS_2. This is due to the formation of MoS_2 nanospheres, which increases the specific surface area. For $MoS_2@WO_{3-x}$, WS_2/MoS_2, and $WS_2/MoS_2@WO_{3-x}$, the dark adsorption experiment results show that MoS_2 nanospheres play a major role in the dark adsorption process. As shown in Table S1, the results of specific surface area measurement correspond to the results of dark adsorption experiment. Under visible light irradiation, compared with other samples, $WS_2/MoS_2@WO_{3-x}$ shows the best visible light photocatalytic degradation performance (~97%). This is because the formation of hierarchical tandem heterojunctions and O doping can effectively inhibit the recombination of photogenerated carriers and prolong the lifetime of photogenerated carriers. Furthermore, the unique core-shell nanosphere structure has more edge active sites. As illustrated in Figure S8, the values of apparent rate constant (k) are determined from the slops of $ln(C/C_0)$ versus t. Obviously, $WS_2/MoS_2@WO_{3-x}$ displays the fastest reaction rate in photocatalytic degradation of 2,4-DCP with the apparent rate constants of $0.03569\,min^{-1}$. The k values of all the composites are enormously higher than those of bare MoS_2, WO_{3-x}, and WS_2. The stability of photocatalysts is of great significance to the practical application of photocatalysts. In order to further verify the degradation performance of $WS_2/MoS_2@WO_{3-x}$ photocatalysts, photocatalytic degradation experiments for MO, MB, and phenol are carried out. As shown in Figure S9a, $WS_2/MoS_2@WO_{3-x}$ photocatalysts have good photocatalytic degradation effect for various pollutants under visible light irradiation. It is helpful to understand the mechanism of photocatalytic degradation by exploring which active groups play the main role in the process of photocatalytic degradation. As shown in Figure S9b, when EDTA-Na and BQ are added to the system, the photocatalytic degradation rate both decreases significantly, which prove that h^+ and ˙O_2^- are the main active groups in the photocatalytic degradation process. In addition, after adding IPA, the photocatalytic degradation rate decreases but not obvious. Therefore, it can be concluded that the order of active groups in photocatalytic degradation is $h^+ > ˙O_2^- > ˙OH$ in this system. Fig. 4d shows the experimental results of $WS_2/MoS_2@WO_{3-x}$

photocatalyst cyclic stability. The $WS_2/MoS_2@WO_{3-x}$ photocatalyst can keep the photocatalytic degradation rate basically stable after four cycles, which indicates that the as-prepared $WS_2/MoS_2@WO_{3-x}$ photocatalyst has good stability. Furthermore, XRD patterns of the $WS_2/MoS_2@WO_{3-x}$ composite before and after four cycles are shown in Figure S10, which indicate that the phase and structure of the used $WS_2/MoS_2@WO_{3-x}$ composite has almost no evident transformation compared with the fresh one. Moreover, as shown in Figure S11, the photocatalytic degradation tests are also carried out in Vis-NIR region. Under Vis-NIR light irradiation, as-prepared $WS_2/MoS_2@WO_{3-x}$ also shows the highest photocatalytic degradation performance for 2,4-DCP. This result further implies that hierarchical tandem heterojunctions and O doping can effectively enhance photodegradation performance in Vis-NIR light region. In addition, as shown in Figure S12, the $WS_2/MoS_2@WO_{3-x}$ photocatalyst also exhibits excellent photocatalytic oxygen evolution performance and remained stable after four cycles of experiments.

Photothermal effect, as an important factor in catalytic reaction, is often neglected. Herein, the photothermal effect is quantitatively investigated by IR thermal driver. There are two main sources of heat energy: 1. Direct thermal radiation. 2. Photothermal effect of semiconductor materials. As shown in Fig. 5a, before irradiation, the initial temperature of photocatalysts is controlled at about 24 °C. After irradiation, the temperature of the photocatalyst is obviously increased (~190 °C), which indicates that the synthesized catalyst has significant photothermal effect and can effectively improve the photocatalytic performance. Compared with conventional large band gap semiconductors, the prepared photocatalysts have strong photothermal effect due to their wide optical absorption range and narrow band gap (Fig. 5b).

In order to further explore the mechanism of as-prepared photocatalyst, electrochemical impedance spectra and transient photocurrent responses experiments are performed to verify the mechanism of separation and transmission of photogenerated carriers. Fig. 6a describes the electrochemical impedance spectra of MoS_2, $MoS_2@WO_{3-x}$, and $WS_2/MoS_2@WO_{3-x}$ composites. It can be seen that the diameters of the arc radius for all of the composites are smaller than MoS_2 electrode. The results show that the formation of tandem heterojunctions can inhibit
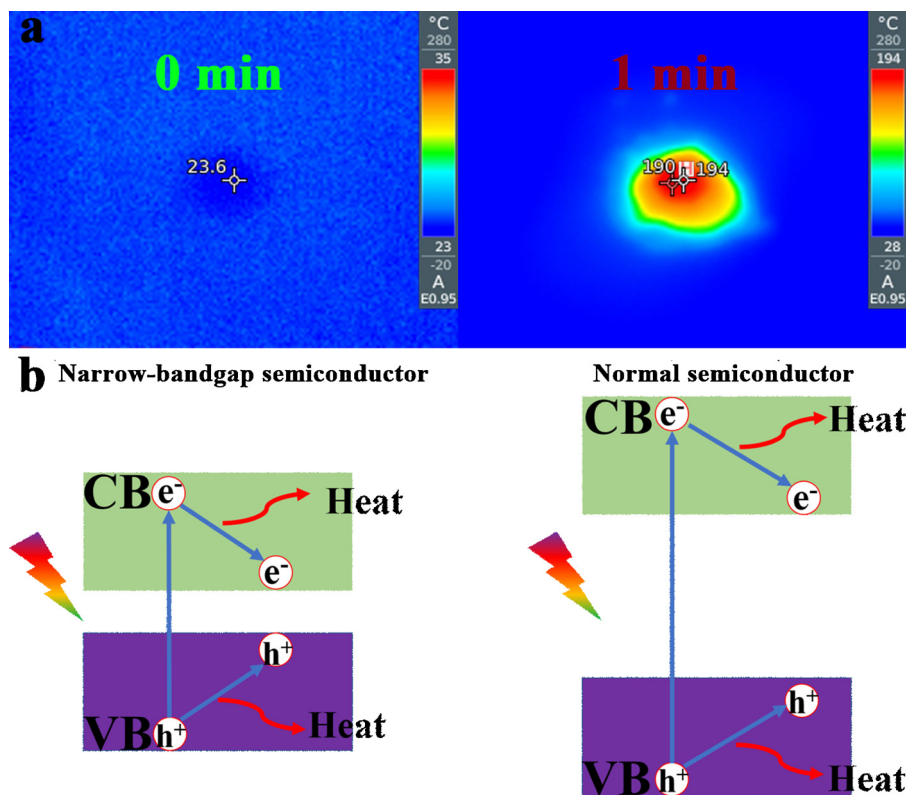
Fig. 5. IR images (a) of $WS_2/MoS_2@WO_{3-x}$ and illustration of the electron-hole generation and relaxation in a narrow-bandgap semiconductor nanocrystal and a normal semiconductor (b).
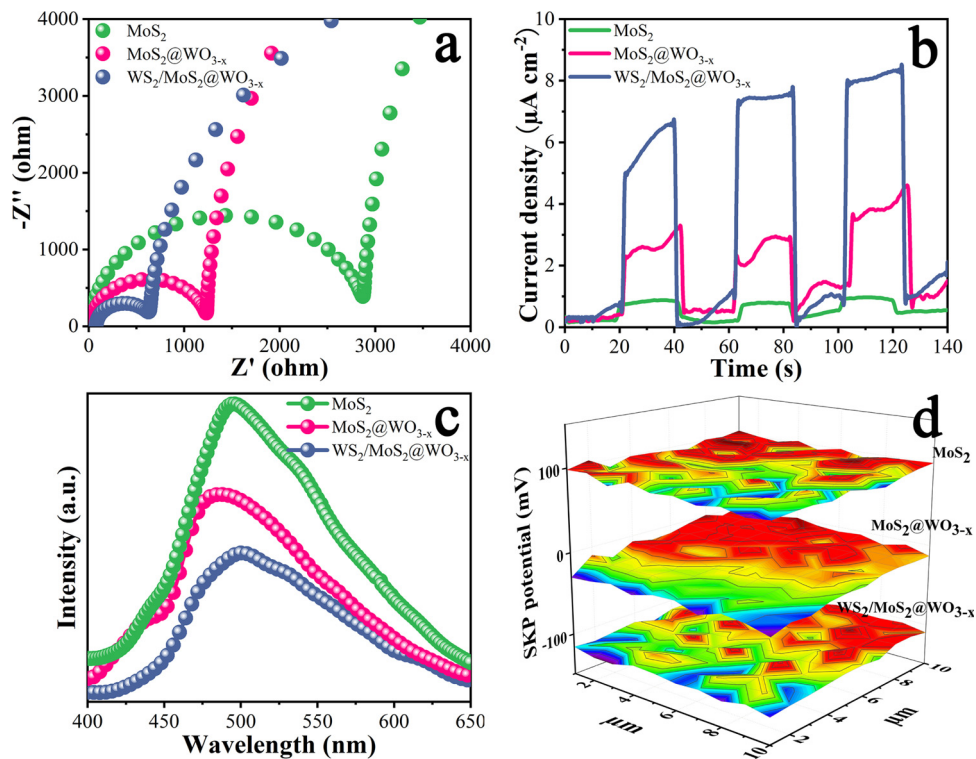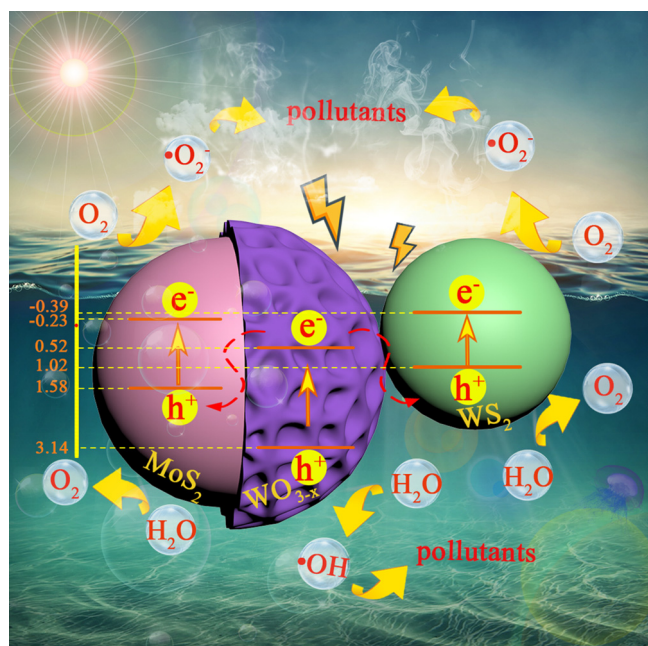

Fig. 6. Electrochemical impedance spectra (a), transient photocurrent responses (b), PL spectra (c), work functions (d), of MoS_2, $MoS_2@WO_{3-x}$, and $WS_2/MoS_2@WO_{3-x}$, respectively.
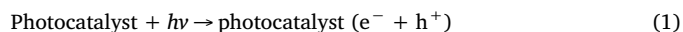
Scheme 2. Schematic description of the proposed mechanism of electron-hole separation and photocatalytic reaction on $WS_2/MoS_2@WO_{3-x}$ hierarchical tandem heterojunctions.

accumulate in the VB of WO_{3-x}. Therefore, the holes remained in the VB of WO_{3-x} have enough energy to degrade pollutants or oxidize H_2O to form ˙OH radicals. And ˙OH subsequently participates in the removal of organic contaminants. WO_{3-x} in this system acts as a bridge to connect two suitable light harvesting semiconductors into an integrated tandem system. The particulate tandem heterojunction structures greatly facilitate the charge separation and effectively suppressing the electron-hole recombination. Moreover, the $WS_2/MoS_2@WO_{3-x}$ tandem heterojunction can effectively harvest sunlight from UV–vis to infrared light. In brief, it may be summarized that the photocatalytic reaction of designed $WS_2/MoS_2@WO_{3-x}$ compound follows a dual Z-scheme mechanism. This photocatalyst can not only favor the spatial separation and transfer of photoinduced charges but also reserve the strong redox capacity in degrading organic contaminants efficiently. The photocatalytic process should be including the following Eqs. (1)–(3).

$$Photocatalyst + h\nu \rightarrow photocatalyst\ (e^- + h^+) \tag{1}$$

$$O_2 + e^- \rightarrow \cdot O_2^- \tag{2}$$

$$h^+/\cdot O_2^-/\cdot OH + 2,4\text{-}DCP \rightarrow degraded\ products \tag{3}$$

4. Conclusions

In summary, a novel $WS_2/MoS_2@WO_{3-x}$ tandem heterojunction was prepared via facile two-step solvothermal and calcination strategy. $WS_2/MoS_2@WO_{3-x}$ heterojunction showed excellent photocatalytic degradation performance for 2,4-DCP, phenol, MO and MB. This excellent photocatalytic performance could be attributed to the following three reasons: (1) The nanospheres were formed by the stacking of lamellar MoS_2, which had a large number of edge active sites and a large specific surface area, thus increasing the reaction and adsorption sites. (2) O doping and tandem heterojunction formation were conducive to the spatial separation and transfer of photogenerated carriers, which made it easier for photogenerated carriers to aggregate on the surface of catalysts and participate in the reaction. (3) The prepared black photocatalysts had broad-spectrum response, which increased the absorption and utilization of light, and had photothermal effect to promote photocatalytic reaction.

Conflict of interest

Nothing declared.

Appendix A. Supplementary data

Supplementary material related to this article can be found, in the online version, at doi:https://doi.org/10.1016/j.apcatb.2019.117913.

the recombination of photogenerated carriers, which is beneficial to the separation and transmission of photogenerated carriers. Fig. 6b shows the transient photocurrent intensities of MoS_2, $MoS_2@WO_{3-x}$, and $WS_2/MoS_2@WO_{3-x}$ composites with repeating on-off cycles under visible-light irradiation. It is clearly that the $MoS_2@WO_{3-x}$, and $WS_2/MoS_2@WO_{3-x}$ composites show enhanced photocurrent intensities. Compared with other samples, $WS_2/MoS_2@WO_{3-x}$ has the largest photocurrent response, which indicates that $WS_2/MoS_2@WO_{3-x}$ has the most effective separation of photogenerated carriers. This corresponds to the above EIS results. Furthermore, PL is a strong evidence to prove the recombination rate of photogenerated carriers in photocatalysts. Fig. 6c displays the PL spectra of MoS_2, $MoS_2@WO_{3-x}$, and $WS_2/MoS_2@WO_{3-x}$ composites under excitation wavelength of 325 nm. It can be seen that the PL spectra of MoS_2 nanospheres shows a strong peak at around 480 nm, which suggests high recombination rate of the photogenerated electron-holes of MoS_2 nanospheres. In contrast, $WS_2/MoS_2@WO_{3-x}$ has the lowest PL intensity, which indicates that the recombination rate of photogenerated carriers is the lowest. This is because the formation of heterojunctions promotes the spatial separation of photogenerated carriers and reduces the recombination of photogenerated carriers. As shown in Fig. 6d, the work function for $WS_2/MoS_2@WO_{3-x}$ heterojunctions is lower than that of MoS_2 nanospheres and $MoS_2@WO_{3-x}$ heterojunction, which ensures the easier escape of electrons from bulk to surface for photocatalysis.

As is detailed discussed above and graphically demonstrated in Scheme 2, the possible charge transfer mechanism is shown as follows. Based on the band gap positions and XPS valence band (Figure S13), it can be calculated that the conduction band (CB) MoS_2, WO_{3-x}, and WS_2 are -0.23, 0.52, and -0.39 eV. It can be inferred that in the hierarchical $WS_2/MoS_2@WO_{3-x}$ tandem heterojunction photocatalyst, the photogenerated charges transfer path would follow the dual Z-scheme mechanism. WS_2, MoS_2 and WO_{3-x} can produce photoinduced electron-hole pairs under visible light irradiation on account of their appropriate band gaps. Then the photoexcited electrons would migrate from the CB of WO_{3-x} to the VB of MoS_2 and WS_2, respectively. Then the electrons would recombine with the holes in the VB of MoS_2 and WS_2, respectively. Eventually, photogenerated electrons aggregate in the CB of MoS_2 and WS_2. In the meanwhile, photoinduced holes would

References

[1] X. Liu, J. Iocozzia, Y. Wang, X. Cui, Y. Chen, S. Zhao, Z. Li, Z. Lin, Noble metal-metal oxide nanohybrids with tailored nanostructures for efficient solar energy conversion, photocatalysis and environmental remediation, Energy Environ. Sci. 10 (2017) 402–434.
[2] N. Meng, J. Ren, Y. Liu, Y. Huang, T. Petit, B. Zhang, Engineering oxygen-containing and amino groups into two-dimensional atomically-thin porous polymeric carbon nitrogen for enhanced photocatalytic hydrogen production, Energy Environ.

Sci. 11 (2018) 566–571.

[3] M.Z. Rahman, C.W. Kwong, K. Davey, S.Z. Qiao, 2D phosphorene as a water splitting photocatalyst: fundamentals to applications, Energy Environ. Sci. 9 (2016) 709–728.

[4] D. Zhang, C. Lee, H. Javed, P. Yu, J.-H. Kim, P.J.J. Alvarez, Easily recoverable, micrometer-sized TiO2 hierarchical spheres decorated with cyclodextrin for enhanced photocatalytic degradation of organic micropollutants, Environ. Sci. Technol. 52 (2018) 12402–12411.

[5] C. Zhang, Y. Zhou, J. Bao, J. Fang, S. Zhao, Y. Zhang, X. Sheng, W. Chen, Structure regulation of ZnS@g-C3N4/TiO2 nanospheres for efficient photocatalytic H2 production under visible-light irradiation, Chem. Eng. J. 346 (2018) 226–237.

[6] Z. Liang, S. Bai, P. Hao, Y. Guo, Y. Xue, J. Tian, H. Cui, Full solar spectrum photocatalytic oxygen evolution by carbon-coated TiO2 hierarchical nanotubes, Appl. Catal. B 243 (2019) 711–720.

[7] W. Zhou, T. Li, J.Q. Wang, Y. Qu, K. Pan, Y. Xie, G.H. Tian, L. Wang, Z.Y. Ren, B.J. Jiang, H.G. Fu, Composites of small Ag clusters confined in the channels of well-ordered mesoporous anatase TiO2 and their excellent solar-light-driven photocatalytic performance, Nano Res. 7 (2014) 731–742.

[8] A. Politano, P. Argurio, G. Di Profio, V. Sanna, A. Cupolillo, S. Chakraborty, H.A. Arafat, E. Curcio, Photothermal membrane distillation for seawater desalination, Adv. Mater. 29 (2017) 1603504.

[9] M. Ye, J. Jia, Z. Wu, C. Qian, R. Chen, P.G. O'Brien, W. Sun, Y. Dong, G.A. Ozin, Synthesis of black TiOx nanoparticles by Mg reduction of TiO2 nanocrystals and their application for solar water evaporation, Adv. Energy Mater. 7 (2017) 1601811.

[10] L.P. Ren, W. Zhou, B.J. Sun, H.Z. Li, P.Z. Qiao, Y.C. Xu, J.X. Wu, K. Lin, H.G. Fu, Defects-engineering of magnetic gamma-Fe2O3 ultrathin nanosheets/mesoporous black TiO2 hollow sphere heterojunctions for efficient charge separation and the solar-driven photocatalytic mechanism of tetracycline degradation, Appl. Catal. B 240 (2019) 319–328.

[11] P. Qiao, J. Wu, H. Li, Y. Xu, L. Ren, K. Lin, W. Zhou, Plasmon Ag-promoted solar-thermal conversion on floating carbon cloth for seawater desalination and sewage disposal, ACS Appl. Mater. Interfaces 11 (2019) 7066–7073.

[12] Z. Gan, X. Wu, M. Meng, X. Zhu, L. Yang, P.K. Chu, Photothermal contribution to enhanced photocatalytic performance of graphene-based nanocomposites, ACS Nano 8 (2014) 9304–9310.

[13] Y. Li, Z. Yin, G. Ji, Z. Liang, Y. Xue, Y. Guo, J. Tian, X. Wang, H. Cui, 2D/2D/2D heterojunction of Ti3C2 MXene/MoS2 nanosheets/TiO2 nanosheets with exposed (001) facets toward enhanced photocatalytic hydrogen production activity, Appl. Catal. B 246 (2019) 12–20.

[14] X. Hu, S. Lu, J. Tian, N. Wei, X. Song, X. Wang, H. Cui, The selective deposition of MoS2 nanosheets onto (101) facets of TiO2 nanosheets with exposed (001) facets and their enhanced photocatalytic H2 production, Appl. Catal. B 241 (2019) 329–337.

[15] M. Wang, P. Ju, J. Li, Y. Zhao, X. Han, Z. Hao, Facile synthesis of MoS2/g-C3N4/GO ternary heterojunction with enhanced photocatalytic activity for water splitting, ACS Sustainable Chem. Eng. 5 (2017) 7878–7886.

[16] W. Yin, L. Yan, J. Yu, G. Tian, L. Zhou, X. Zheng, X. Zhang, Y. Yong, J. Li, Z. Gu, Y. Zhao, High-throughput synthesis of single-Layer MoS2 nanosheets as a near-infrared photothermal-triggered drug delivery for effective cancer therapy, ACS Nano 8 (2014) 6922–6933.

[17] S.S. Chou, B. Kaehr, J. Kim, B.M. Foley, M. De, P.E. Hopkins, J. Huang, C.J. Brinker, V.P. Dravid, Chemically exfoliated MoS2 as near-infrared photothermal agents, Angew. Chem., Int. Ed. 52 (2013) 4160–4164.

[18] X.-H. Zhang, N. Li, J. Wu, Y.-Z. Zheng, X. Tao, Defect-rich O-incorporated 1T-MoS2 nanosheets for remarkably enhanced visible-light photocatalytic H2 evolution over CdS: The impact of enriched defects, Appl. Catal. B 229 (2018) 227–236.

[19] Z. Li, X. Meng, Z. Zhang, Recent development on MoS2-based photocatalysis: A review, J. Photochem. Photobiol. C Photochem. Rev. 35 (2018) 39–55.

[20] M. Donarelli, L. Ottaviano, 2D materials for gas sensing applications: a review on graphene oxide, MoS2, WS2 and phosphorene, Sensors 18 (2018) 3638.

[21] D.P. Kumar, S. Hong, D.A. Reddy, T.K. Kim, Ultrathin MoS2 layers anchored exfoliated reduced graphene oxide nanosheet hybrid as a highly efficient cocatalyst for CdS nanorods towards enhanced photocatalytic hydrogen production, Appl. Catal. B 212 (2017) 7–14.

[22] R.K. Chava, J.Y. Do, M. Kang, Smart hybridization of Au coupled CdS nanorods with few layered MoS2 nanosheets for high performance photocatalytic hydrogen evolution reaction, ACS Sustainable Chem. Eng. 6 (2018) 6445–6457.

[23] B. Guo, K. Yu, H. Fu, Q. Hua, R. Qi, H. Li, H. Song, S. Guo, Z. Zhu, Firework-shaped TiO2 microspheres embedded with few-layer MoS2 as an anode material for excellent performance lithium-ion batteries, J. Mater. Chem. A Mater. Energy Sustain. 3 (2015) 6392–6401.

[24] T. Zhao, Z. Xing, Z. Xiu, Z. Li, S. Yang, W. Zhou, Oxygen-doped MoS2 nanospheres/CdS quantum dots/g-C3N4 nanosheets super-architectures for prolonged charge lifetime and enhanced visible-light-driven photocatalytic performance, ACS Appl. Mater. Interfaces 11 (2019) 7104–7111.

[25] D.P. Wu, Y.X. Wang, F.J. Wang, H.J. Wang, Y.P. An, Z.Y. Gao, F. Xu, K. Jiang, Oxygen-incorporated few-layer MoS2 vertically aligned on three-dimensional graphene matrix for enhanced catalytic performances in quantum dot sensitized solar cells, Carbon 123 (2017) 756–766.

[26] T.H. Sun, Z.P. Li, X.H. Liu, L.M. Ma, J.Q. Wang, S.R. Yang, Oxygen-incorporated MoS2 microspheres with tunable interiors as novel electrode materials for supercapacitors, J. Power Sources 352 (2017) 135–142.

[27] M.B. Tahir, M. Sagir, K. Shahzad, Removal of acetylsalicylate and methyl-theobromine from aqueousenvironment using nano-photocatalyst WO3-TiO2@g-C3N4 composite, J. Hazard. Mater. 363 (2019) 205–213.

[28] C. Sotelo-Vazquez, R. Quesada-Cabrera, M. Ling, D.O. Scanlon, A. Kafizas, P.K. Thakur, T.-L. Lee, A. Taylor, G.W. Watson, R.G. Palgrave, J.R. Durrant, C.S. Blackman, I.P. Parkin, Evidence and effect of photogenerated charge transfer for enhanced photocatalysis in WO3/TiO2 heterojunction films: A computational and experimental study, Adv. Funct. Mater. 27 (2017) 1605413.

[29] W. Shi, X. Guo, C. Cui, K. Jiang, Z. Li, L. Qu, J.-C. Wang, Controllable synthesis of Cu2O decorated WO3 nanosheets with dominant (001) facets for photocatalytic CO2 reduction under visible -light irradiation, Appl. Catal. B 243 (2019) 236–242.

[30] S. Adhikari, D. Sarkar, H.S. Maiti, Synthesis and characterization of WO3 spherical nanoparticles and nanorods, Mater. Res. Bull. 49 (2014) 325–330.

[31] X.L. Zhang, X. Wang, D.F. Wang, J.H. Ye, Conformal BiVO4-layer/WO3-nanoplate-array heterojunction photoanode modified with cobalt phosphate cocatalyst for significantly enhanced photoelectrochemical performances, ACS Appl. Mater. Interfaces 11 (2019) 5623–5631.

[32] L. Zhang, H. Zhang, B. Wang, X. Huang, Y. Ye, R. Lei, W. Feng, P. Liu, A facile method for regulating the charge transfer route of WO3/CdS in high-efficiency hydrogen production, Appl. Catal. B 244 (2019) 529–535.

[33] S.L. Wang, Y. Zhu, X. Luo, Y. Huang, J. Chai, T.I. Wong, G.Q. Xu, 2D WC/WO3 heterogeneous hybrid for photocatalytic decomposition of organic compounds with Vis-NIR Light, Adv. Funct. Mater. 28 (2018) 1705357.

[34] Z.F. Huang, J.J. Song, L. Pan, X.W. Zhang, L. Wang, J.J. Zou, Tungsten oxides for photocatalysis, electrochemistry, and phototherapy, Adv. Mater. 27 (2015) 5309–5327.

[35] Y. Zhong, G. Zhao, F. Ma, Y. Wu, X. Hao, Utilizing photocorrosion-recrystallization to prepare a highly stable and efficient CdS/WS2 nanocomposite photocatalyst for hydrogen evolution, Appl. Catal. B 199 (2016) 466–472.

[36] J.P. Zou, J. Ma, J.M. Luo, J. Yu, J.K. He, Y.T. Meng, Z. Luo, S.K. Bao, H.L. Liu, S.L. Luo, X.B. Luo, T.C. Chen, S.L. Suib, Fabrication of novel heterostructured few layered WS2-Bi2WO6/Bi3.84W0.16O6.24 composites with enhanced photocatalytic performance, Appl. Catal. B 179 (2015) 220–228.

[37] P. Atkin, T. Daeneke, Y. Wang, B.J. Carey, K.J. Berean, R.M. Clark, J.Z. Ou, A. Trinchi, I.S. Cole, K. Kalantar-zadeh, 2D WS2/carbon dot hybrids with enhanced photocatalytic activity, J. Mater. Chem. A Mater. Energy Sustain. 4 (2016) 13563–13571.

[38] M. Gopannagari, D.P. Kumar, D.A. Reddy, S. Hong, M.I. Song, T.K. Kim, In situ preparation of few-layered WS2 nanosheets and exfoliation into bilayers on CdS nanorods for ultrafast charge carrier migrations toward enhanced photocatalytic hydrogen production, J. Catal. 351 (2017) 153–160.

[39] T. Zhao, Z. Xing, Z. Xiu, Z. Li, P. Chen, Q. Zhu, W. Zhou, Synergistic effect of surface plasmon resonance, Ti3+ and oxygen vacancy defects on Ag/MoS2/TiO2-x ternary heterojunctions with enhancing photothermal catalysis for low-temperature wastewater degradation, J. Hazard. Mater. 364 (2019) 117–124.

[40] H. Lin, Y. Li, H. Li, X. Wang, Multi-node CdS hetero-nanowires grown with defect-rich oxygen-doped MoS2 ultrathin nanosheets for efficient visible-light photocatalytic H2 evolution, Nano Res. 10 (2017) 1377–1392.

[41] Y. Li, K. Chang, H. Tang, B. Li, Y. Qin, Y. Hou, Z. Chang, Preparation of oxygen-deficient WO3-x nanosheets and their characterization as anode materials for high-performance Li-ion batteries, Electrochim. Acta 298 (2019) 640–649.

[42] X. Yan, M. Xia, B. Xu, J. Wei, B. Yang, G. Yang, Fabrication of novel all-solid-state Z-scheme heterojunctions of 3DOM-WO3/Pt coated by mono-or few-layered WS2 for efficient photocatalytic decomposition performance in Vis-NIR region, Appl. Catal. B 232 (2018) 481–491.

[43] H. Khan, M.G. Rigamonti, D.C. Boffito, Enhanced photocatalytic activity of Pt-TiO2/WO3 hybrid material with energy storage ability, Appl. Catal. B 252 (2019) 77–85.

[44] S. Luo, S. Dong, C. Lu, C. Yu, Y. Ou, L. Luo, J. Sun, J. Sun, Rational and green synthesis of novel two-dimensional WS2/MoS2 heterojunction via direct exfoliation in ethanol-water targeting advanced visible-light-responsive photocatalytic performance, J. Colloid Interface Sci. 513 (2018) 389–399.